Check for updates

Large-scale planar and spherical light-emitting diodes based on arrays of perovskite quantum wires

Daquan Zhang [1], Qianpeng Zhang[1], Beitao Ren[1], Yudong Zhu [1,2], Mohamed Abdellah[3,4], Yu Fu[1], Bryan Cao[1], Chen Wang[1], Leilei Gu[1], Yucheng Ding[1], Kwong-Hoi Tsui[1], Sufeng Fan[5], Swapnadeep Poddar[1], Lei Shu[1], Yuting Zhang[1], Dai-Bin Kuang [6], Jin-Feng Liao[6], Yang Lu [5], Kaibo Zheng [3,7], Zhubing He[2] and Zhiyong Fan [1,8 ✉]

Halide perovskites are enticing candidates for highly efficient planar light-emitting diodes (LEDs) with commercial potential in displays and lighting. However, it remains a challenge for conventional solution fabrication processes to fabricate large-scale or non-planar LEDs due to the non-uniformity of perovskite films in conjunction with material stability issues. Here large-area highly uniform arrays of crystalline perovskite quantum wires are grown with emission spectra covering the whole visible range. Photoluminescence quantum yield of up to 92% and 5,644 hours as the time for photoluminescence to degrade down to its 50% of the initial value under ambient conditions are achieved for MAPbBr$_3$ quantum wires. LEDs based on these quantum wires on rigid and flexible planar substrates are fabricated up to a four-inch wafer size and also unique three-dimensional spherical LEDs with outstanding uniformity are reported. The results suggest that the approach developed here can be generalized to other unconventional three-dimensional LEDs in the future.

Metal halide perovskite (MHP) materials have been widely explored for efficient light-emitting diodes (LEDs) because of their marvellous figures of merit such as facile synthesis, efficient radiative recombination, remarkable colour purity and bandgap tunability[1–3]. Prevailing approaches to boost LED performance include improving the materials' photoluminescence quantum yield (PLQY) by reducing the grain size to enhance the spatial excitonic confinement (the quantum confinement effect[4–6]) and passivating the grain boundary to suppress non-radiative recombination[7]. Even though a close-to-unity PLQY has been obtained for colloidal perovskite quantum dots (QDs)[4], only a fraction of emitted light (<50%) can escape from a solid QD film because of poor light out-coupling efficiency (OCE)[8]. A general route to fabricate different MHPs with high PLQY and tunable photoluminescence (PL) colours (red, green and blue, at least) is indispensable for displays and lighting. Furthermore, the fabrication process of conventional MHP LEDs relies on solution spin coating, which is preferably performed in a glovebox due to the material's intrinsic low resistance to humidity[9]. In conjunction with substrate-size constraints, it is challenging to use the widely adopted spin-coating method to manufacture large-area LEDs with good uniformity. Furthermore, the mainstream spin-coating method is certainly incompatible with three-dimensional (3D) substrates, and thus, no 3D MHP LED has been demonstrated hitherto, to the best of our knowledge. However, most light sources in nature—from stars to fireflies—have 3D geometry, irrespective of their size. They are advantageous over planar counterparts on many aspects, especially spatial uniformity in the distribution of luminance.

Here we demonstrate highly uniform crystalline perovskite quantum-wire (QW) arrays in hydrophobic porous alumina membranes (PAMs) for LEDs, via a close-spaced vapour reaction (CSVR) method. Benefiting from the generic growth approach, both organic and inorganic mixed-halide-perovskite-based QWs, namely, APbX$_3$ (A = Cs or methylamine (MA); X = I, Br, Cl or a combination), are successfully grown on both large-scale planar and 3D spherical substrates, with PL colours covering the whole visible range (blue, cyan, green and red). MAPbBr$_3$ QW arrays show a 92% PLQY and the time to reach 50% PL (T_{PL50}) of 5,644 h under ambient conditions. They are fabricated into planar LEDs with a high peak luminance of 31,667 cd m^{-2} and long lifetime of 16.9 h in the ambient environment. Benefiting from the scalability of PAM fabrication, the CSVR process and hole-transport-layer (HTL) evaporation, excellent up-scalability of MAPbBr$_3$ QWs LEDs is demonstrated with the successful fabrication of four-inch wafer-scale LED devices with respectable electroluminescence (EL) uniformity. Intriguingly, the conformal nature of CSVR QW growth enables the fabrication of a unique 3D spherical LED device, demonstrating excellent spatial EL luminance distribution.
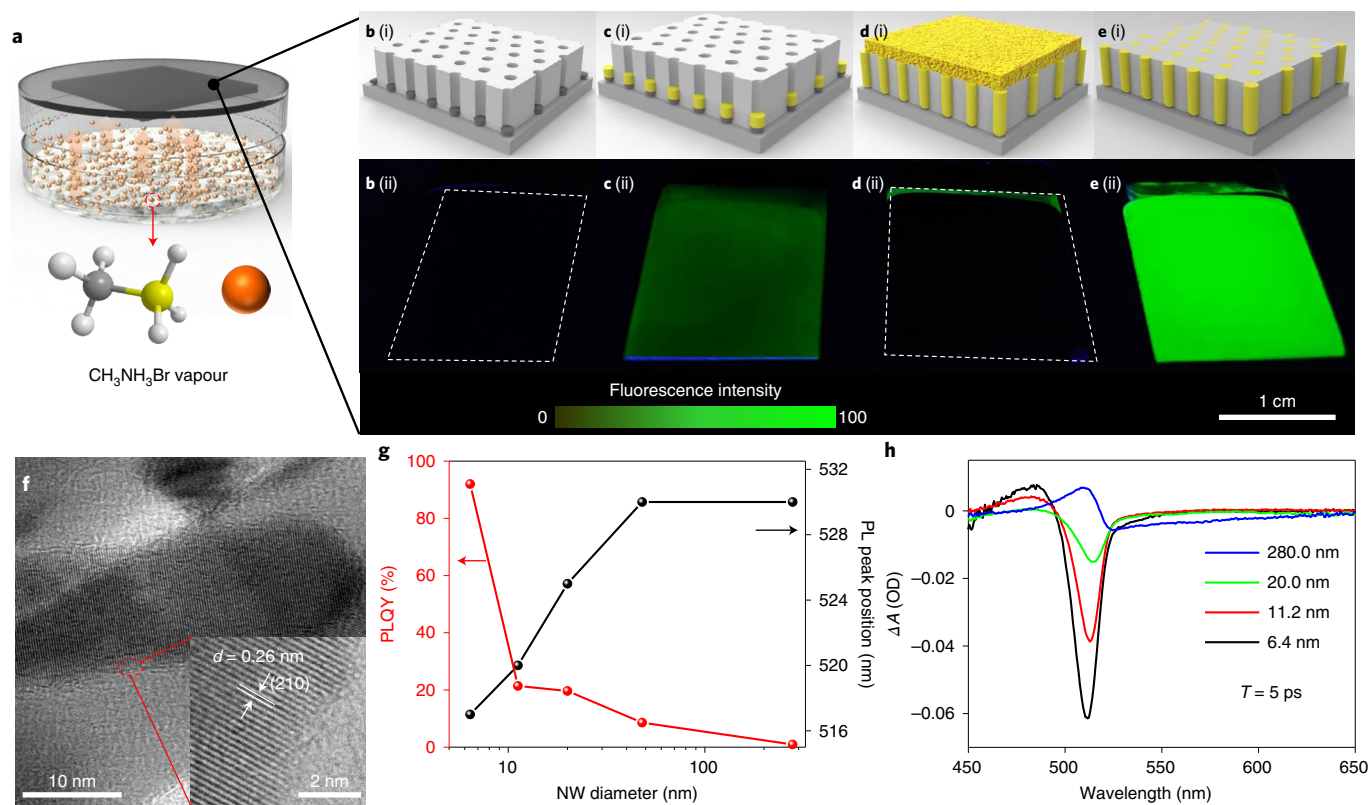
Results

Figure 1a shows a schematic of the typical CSVR growth setup for MAPbBr$_3$ QWs. It starts from a PAM (Fig. 1b) whose average pore diameter can be extracted as 6.4 nm (Supplementary Fig. 1). There are three consecutive steps to obtain QW arrays with high PLQY: initial growth with weak PL (Fig. 1c(i)(ii)), overgrowth with indiscernible PL (Fig. 1d(i)(ii)) and removing the polycrystalline

Fig. 1 | Growth and characterization of MAPbBr₃ QW arrays. a, Schematic of the CSVR setup. **b–e**, Schematic (top) and fluorescent images (bottom) of the chip during different growth steps: before growth (**b**), little growth (**c**), overgrowth (**d**) and clean surface (**e**). The effective chip area is around 1.5 cm × 2.0 cm. **f**, HRTEM image of a single QW extracted from PAM. **g**, PLQY and PL peak position of NW arrays with diameters decreasing from the bulk (280.0 nm) to quantum (6.4 nm) regime. **h**, TA spectra of NW arrays with different diameters at the same delay time of 5 ps.

perovskite film on the surface by an ion-milling process (Methods) to achieve bright PL (Fig. 1e(i)(ii)). A cross-sectional scanning electron microscopy (SEM) image of the QW arrays in PAM is shown in Supplementary Fig. 2a. High-resolution transmission electron microscopy (HRTEM) images of a single MAPbBr₃ QW (Fig. 1f) and X-ray diffraction (XRD) pattern of QW arrays (Supplementary Fig. 2c) reveal its crystalline nature. When decreasing the diameter of the nanowires (NWs) from 280.0 nm (bulk wire) to 6.4 nm (QWs), the PL peak gradually shifts from 530 to 517 nm, along with the significantly boosted PLQY (Fig. 1g). The maximum absolute PLQY of 92% is one of the highest recorded values for any MAPbBr₃ solid-state film, to the best of our knowledge[8]. Such an enormous improvement is attributed to quantum confinement, namely, spatial confinement, of the wave function of the photogenerated electrons and holes, culminating in the engendered radiative recombination rate[10–12]. Meanwhile, PAMs can also provide 3D surface passivation[13] to the QWs, which is confirmed by the X-ray photoelectron spectroscopy data (Supplementary Fig. 5). Further, the relatively low refractive index of alumina substantially increases the light OCE of QW arrays up to 97.8% (Supplementary Fig. 6). Transient absorption (TA) measurement is also conducted to study the photoexcitation and energy transfer dynamics in QWs. Supplementary Fig. 7a–d shows the TA mappings of different QW arrays after pulse excitation as a function of both wavelength and delay time, from which the TA spectra (Fig. 1h) and dynamic TA signals (Supplementary Fig. 7e) can be extracted. It is clear that a ground-state bleach (GSB) peak becomes more distinctive when reducing the NW diameter into the quantum regime (6.4 nm). Meanwhile, a much longer TA-signal decay time (Supplementary Table 1) for 6.4 nm QWs reveals strong radiative carrier recombination, which is consistent with the high

PLQY value. Under such consideration, all the QWs used subsequently have a diameter of 6.4 nm, if mentioned otherwise.

To demonstrate growth generalization, all-inorganic CsPbBr₃ (Supplementary Fig. 9) and mixed halide QWs are also grown using CsPbBr₃ and mixed halide sources, respectively, in a similar CSVR process (Methods). Figure 2a shows the PL spectra of four different MAPbX₃ QWs that cover the whole visible range (blue, cyan, green and red) with a full-width at half-maximum of 21 nm for blue and green. Figure 2b shows the fluorescent photographs of the corresponding four-inch wafer-scale MAPbBr₃ QWs on a rigid substrate with excellent brightness and uniformity. Meanwhile, considering the excellent mechanical flexibility of thin PAM[13], four-inch wafer-scale flexible QW arrays are grown on two types of flexible substrate: thin Al foils (50 μm thick) (Fig. 2c) and Corning Willow glass (100 μm thick) (Fig. 2d).

Recently, poor mechanical stability of perovskite-based devices has been reported, which was attributed to the weak adhesion between the perovskite layer and substrates[14]. In contrast, our perovskite QWs are grown in PAM nanochannels and hence have strong adhesion with the supporting substrate. To vividly demonstrate it, an adhesive tape-assisted peel-off process is executed. As shown in Fig. 3a, the PL of thermally evaporated perovskite thin film on indium tin oxide (ITO) glass almost vanishes after 300 cycles because of material delamination (Supplementary Fig. 10). On the contrary, for the QWs in PAM, there is no obvious PL signal drop after 1,000 peel-off cycles. The cohesion energy, G_c, of QWs in PAMs is further measured be to 12.4 J m⁻² (Fig. 3b and Supplementary Fig. 11), which is significantly higher than any of the reported perovskite thin films (to the best of our knowledge)[15]. This strong adhesion makes it promising for mechanically stable
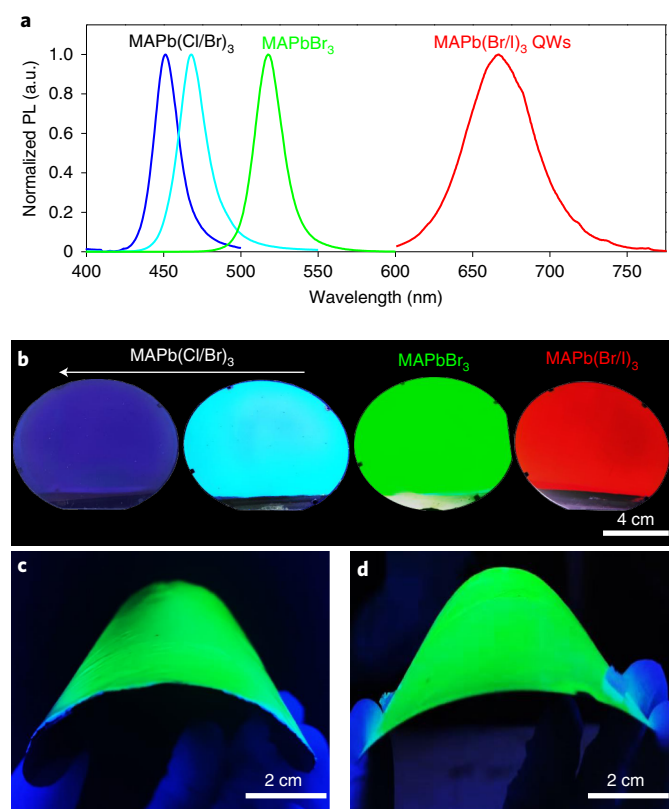
Fig. 2 | Growth generalization and flexibility demonstration of MAPbX₃ QWs. a,b, Growth generalization of perovskite QW arrays: PL spectra (**a**) and corresponding four-inch wafer-scale fluorescent images (**b**) of MAPb(Cl/Br)₃, MAPbBr₃ and MAPb(Br/I)₃ QW arrays. **c,d**, Flexibility demonstration: fluorescent photographs of four-inch wafer-scale MAPbBr₃ QWs on bent ultrathin Al foil (**c**) and Corning Willow glass (**d**).

optoelectronics. Meanwhile, we have reported that 3D passivation by PAM can improve the stability of MHP NWs[13,16–19]. Here we further carry out hydrophobic treatment on the PAM surface[20] to dramatically increase the water contact angle from 14.3° (Fig. 3c) to 117.3° (Fig. 3d). The as-obtained hydrophobic MAPbBr₃ QW arrays show excellent water-repellent property (Supplementary Video 1). Figure 3e shows a fluorescent image of the hydrophobic QWs with a drop of water on it for 10 min, which does not show obvious evanescence of fluorescence. The stability is quantitatively evaluated by monitoring the integrated PL intensity decay over time (Fig. 3f and Supplementary Fig. 12). Interestingly, there is only 1% drop after five days in ambient air (that is, at 23 °C and ~45–55% relative humidity) and the extrapolated time to drop down to 50% PL (T_{PL50}) is 5,644 h (Supplementary Fig. 13).

Even though a few studies have reported solution-processed perovskite QWs with a high PLQY (>70%), efficient charge-carrier injection uniformly into each QW is still a challenge to implement in LEDs[10,11]. In this regard, our perovskite QW arrays in a robust PAM with high uniformity make it promising if sandwiched between the top and bottom charge-carrier injection layers. A schematic (Fig. 4a) shows a wafer-size device structure, where an ultrathin (~5 nm) Al₂O₃ layer, usually known as a barrier layer[21], works as a tunnelling barrier for electron injection[22,23]. Its existence can be confirmed from the cross-sectional TEM image of the device (Fig. 4b) and the HRTEM images in Supplementary Fig. 14. The active emission layer is MAPbBr₃ QW arrays with QW length of ~200.0 nm and an average diameter of 6.4 nm. A thin layer (~20 nm) of evaporated copper phthalocyanine (CuPc) is used for hole injection and

electron blocking[24]. An indium zinc oxide (IZO) layer is utilized as a transparent top electrode. Figure 4c shows the band diagram of the device. Note that Al/Al₂O₃/perovskite is a metal–insulator–semiconductor (MIS) junction[22,23]. When the bias voltage is high enough to drive electron tunnelling through Al₂O₃, radiative recombination occurs inside MAPbBr₃ QWs to emit light. Supplementary Video 2 shows the real-time measurement of a perovskite LED device with voltage scanning. The EL spectra under different bias voltages are shown in Fig. 4d, where a turn-on voltage of 4.4 V and Commission Internationale de l'éclairage (CIE) colour-space coordinates of (0.094, 0.778) are shown. Figure 4e plots the $\frac{I}{V^2}$ versus $\frac{1}{V}$ with y axis in the log scale, where I is the integrated EL intensity and V is the bias voltage. The perfect linear dependence obviously indicates the carrier-tunnelling mechanism in our LEDs[22,23].

The current density–voltage (J–V) and luminance–voltage (L–V) curves are shown in Fig. 5a. The maximum luminance is 31,667 cd m⁻² at a current density of 477 mA cm⁻² (8 V). Figure 5b shows the EQE–V and current efficiency (CE)–V curves. The maximum EQE and CE are 7.3% and 22 cd A⁻¹, respectively. Note that this EQE value is more than 90 times higher than the previous report in which the MIS junction was also used to inject carriers into a perovskite polycrystalline film[23]. We attribute this dramatic improvement to high material quality of the QWs and carrier spatial confinement, substantially promoting radiative recombination. Figure 5c shows the T_{EL50} values with different initial luminances (L_0). When measured in ambient air, the device has a T_{EL50} value of 2.9 h and 6 s for L_0 values of 193 and 15,662 cd m⁻², respectively. Intriguingly, there is no obvious improvement when measured in the glovebox. Considering the excellent water-repellent property of the QWs in PAM, the EL decay is mainly attributed to ion migration in perovskite materials[25,26]. To suppress it, alternating-current (a.c.) bias has been reported to be an effective approach because of ion recovery and lower heat generation during the negative-bias period[27,28]. Supplementary Fig. 18 shows the time-domain luminance decays for both direct-current (d.c.) and a.c. bias voltages. Figure 5c shows the T_{EL50} values under a.c. bias (1 Hz) with different L_0 values. For a fair comparison, the effective T_{EL50} value of the a.c. mode is the real turn-on time (duty cycle, 50%), namely, half the time required for the luminance to decay to $0.5L_0$. Evidently, the T_{EL50} value is significantly improved from 6 s to 5.8 min for high L_0 (>10,000 cd m⁻²) and from 2.9 to 18.2 h for low L_0 (~100 cd m⁻²). We further tested the frequency effect on device operation (Supplementary Fig. 19).

Benefiting from the scalability of PAM fabrication, CSVR process and HTL evaporation, excellent up-scalability of QW LEDs is demonstrated. Specifically, a 3.5 cm × 5.0 cm EL pattern and two four-inch wafer-scale EL devices without and with extra current distribution gridlines are shown in Fig. 5d–f, respectively. This is the first time that a wafer-scale single-perovskite LED device has ever been reported, to the best of our knowledge. Supplementary Fig. 21 demonstrates the excellent uniformity of QW quality via PL measurement as well as excellent EL uniformity in large scale after adding the gridline electrodes to improve the top-contact current spreading, which is already a common technology used for large-area organic LEDs[29]. The high brightness and uniformity of both PL (Fig. 2b) and EL (Fig. 5f) indicate the great potential of our perovskite QW arrays for display applications in the future. To explore the potency of MAPbBr₃ QWs for mechanically flexible applications, a thin layer of Au (30 nm) is used to replace the rigid IZO top electrode. Further, a flexible LED device with an effective area of 1 cm × 7 cm on the Corning Willow glass is demonstrated in Fig. 5g,h. The EL brightness can be further improved by exploring other flexible transparent electrodes, such as the inkjet-printed Ag grids[30].

Till date, the vast majority of research on LEDs using perovskites or other inorganic semiconductors has been based on planar device
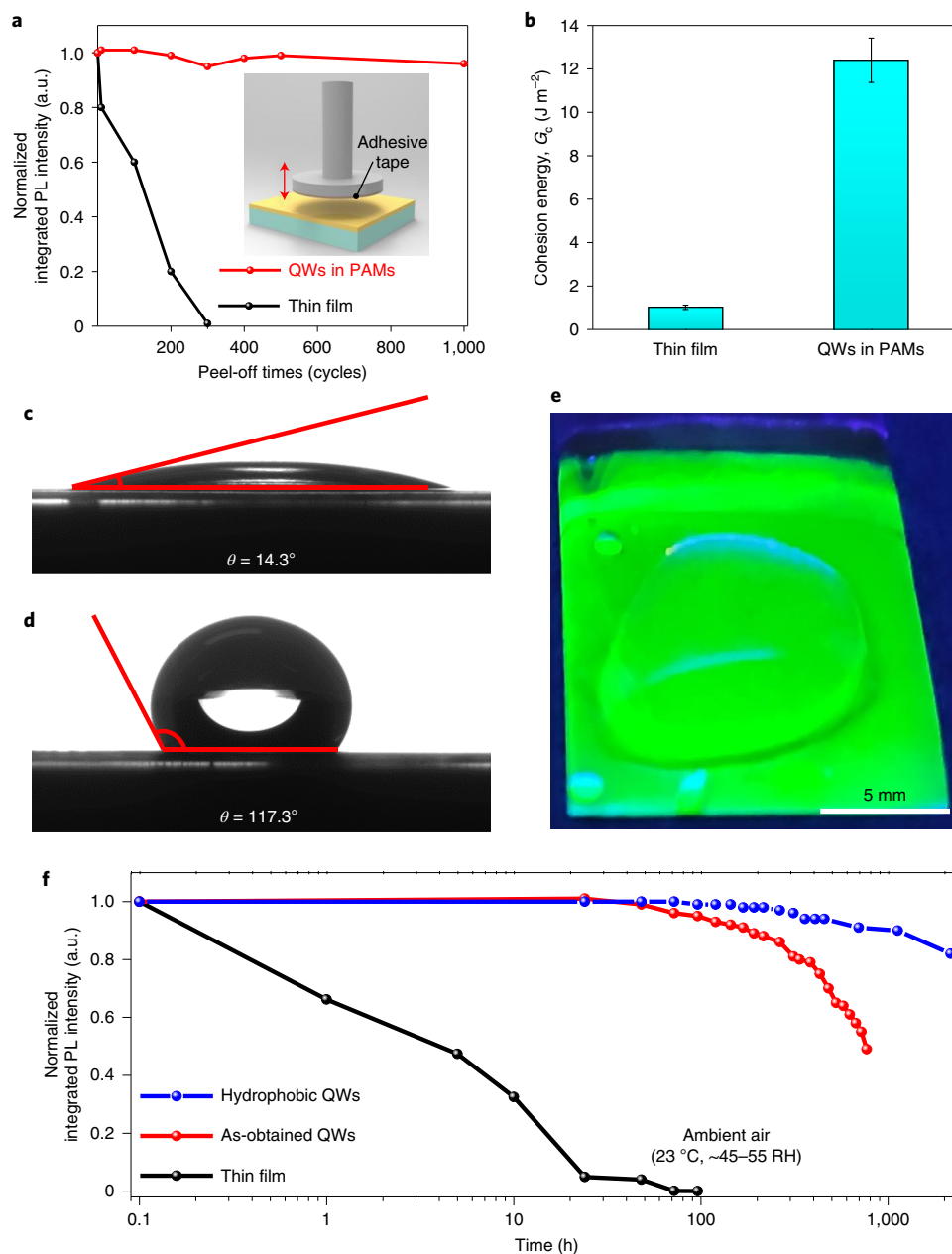
Fig. 3 | Mechanical and environmental stability test of MAPbBr$_3$ thin film and QW arrays. a, Normalized integrated PL intensity evolution of MAPbBr$_3$ thin film and QW arrays over tape-assisted peel-off test cycles. The inset shows a schematic of the test setup. **b**. Calculated cohesion energy G_c of MAPbBr$_3$ thin film and QWs in PAMs. The error bars indicate a standard deviation of ±5%. **c,d**, Water contact angle measurement of PAM without (**c**) and with (**d**) hydrophobic surface treatment. **e**, Fluorescent image of hydrophobic QWs with a drop of water on it after 10 min. **f**, Normalized integrated PL intensity evolution of MAPbBr$_3$ thin film and QW arrays over time in ambient air (at 23 °C and ~45–55% relative humidity). The excitation-light wavelength is 350 nm with a light power density of 5 mW cm^{-2}.

structures, leading to non-uniform spatial distributions of luminance. However, in nature, from stars to fireflies, most light sources have 3D geometry, regardless of their size. Although a 3D light source has many advantages over a planar counterpart (especially on spatially uniform distribution of luminance), suffering from restricted solution processes, it is very challenging to conventionally fabricate non-planar MHP LEDs. In fact, owing to the conformal nature of PAM fabrication and CSVR process, the successful growth of uniform perovskite QWs on an Al sphere with a diameter of 1.5 cm has been achieved (Methods), as shown in Fig. 6a, demonstrating excellent PL uniformity and brightness. In this case,

also to demonstrate the versatility of the CSVR process, CsPbBr$_3$ is used instead of MAPbBr$_3$ (Methods). To identify the optimal condition to fabricate 3D spherical MHP LEDs, a planar device structure, namely, Al/Al$_2$O$_3$/CsPbBr$_3$ QWs/NiO$_x$/IZO (Fig. 6b (inset) and Supplementary Fig. 22), has been initially explored. Note that atomic layer deposition (ALD) is used to deposit p-type NiO$_x$ as the HTL here as it is a highly conformal coating technique having excellent compatibility with 3D substrates. Interestingly, we find that CsPbBr$_3$ QWs can retain a bright PL after annealing at 300 °C in air for 1 h (Supplementary Fig. 23). Figure 6b shows the EL emission peak (under 10 V bias) at 509 nm, with the inset showing the EL image.
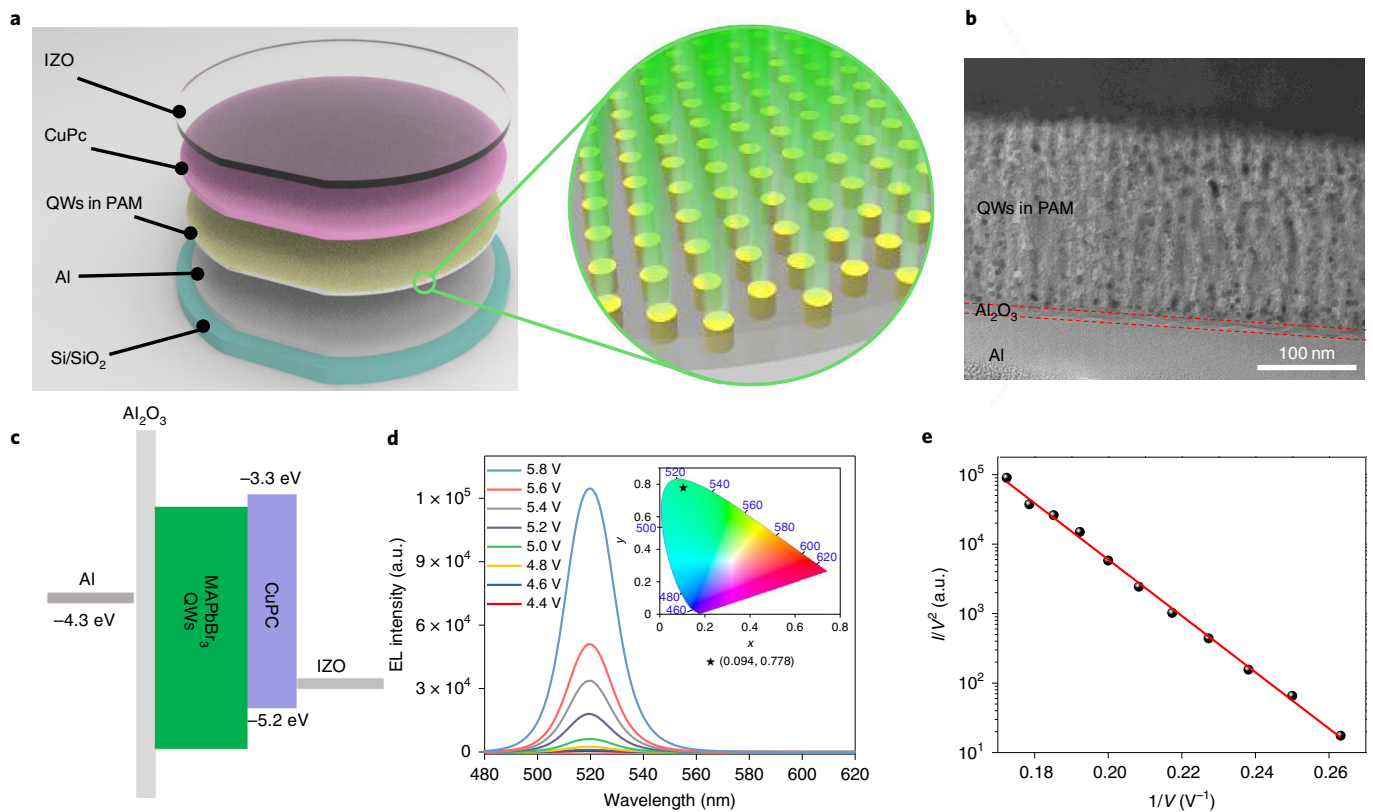
Fig. 4 | MAPbBr$_3$-QW-array-based LED performance. a, Device schematic. **b**, Cross-sectional TEM image showing QWs in PAMs with an ultrathin Al$_2$O$_3$ layer. **c**, Band alignment of the device. **d**, EL spectra under different bias voltages. The inset shows the corresponding CIE colour-space coordinates. **e**, Integrated EL intensity divided by V^2 as a function of the reciprocal bias voltage (1/V). The red line is the linear fitting of the data.
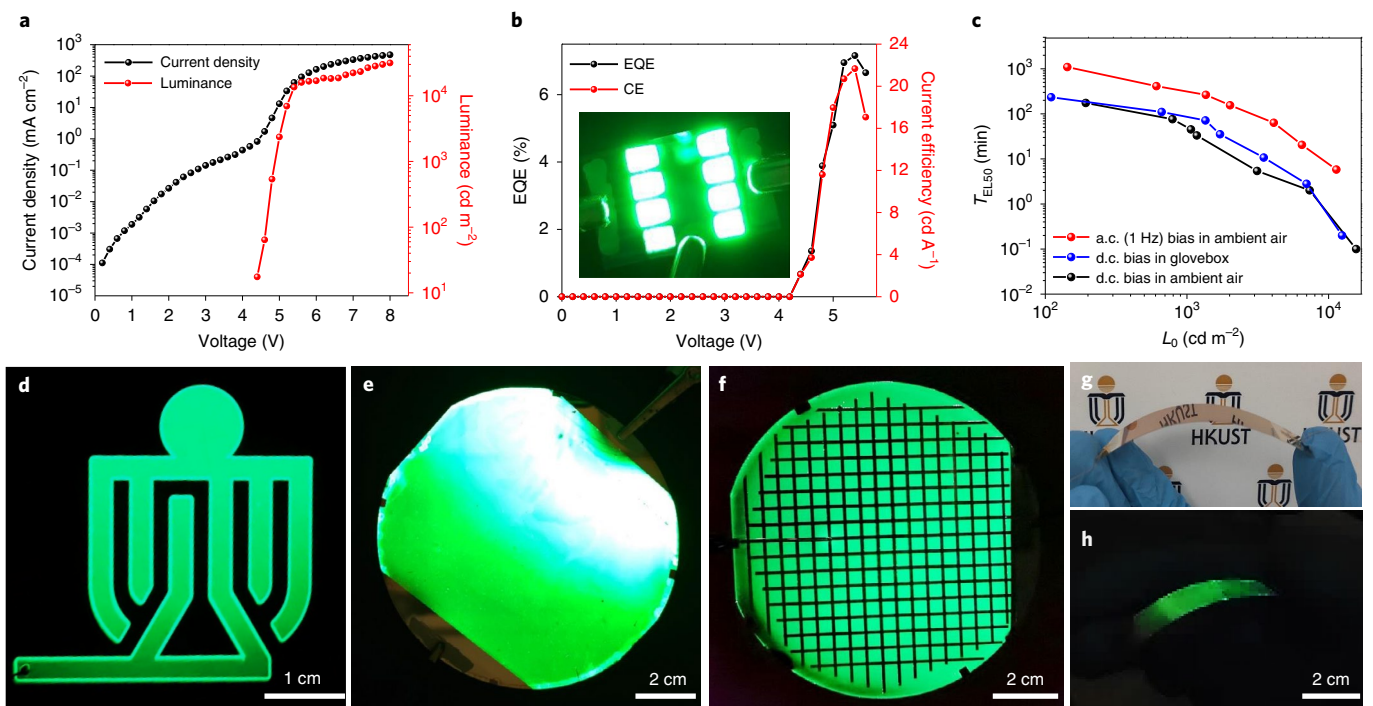
Fig. 5 | MAPbBr$_3$-QW-array-based LED performance. a,b, J–L–V (**a**) and EQE–CE–V (**b**) curves of the best device. The inset in **b** shows an EL image of eight devices illuminated simultaneously. Every single device has a size of 2.0 mm × 2.8 mm. **c**, T_{EL50} as a function of initial luminance (L_0) under different measurement conditions: d.c. bias in the ambient environment (black) and glovebox (blue); a.c. bias (1 Hz) in the ambient environment (red). **d–f**, EL scalability demonstration: a 3 cm × 5 cm display pattern (**d**) and a four-inch wafer-scale device without (**e**) and with (**f**) current distribution gridline electrode. **g,h**, Flexibility demonstration: digital photograph (**g**) and EL image (**h**) of a 1 cm × 7 cm device.
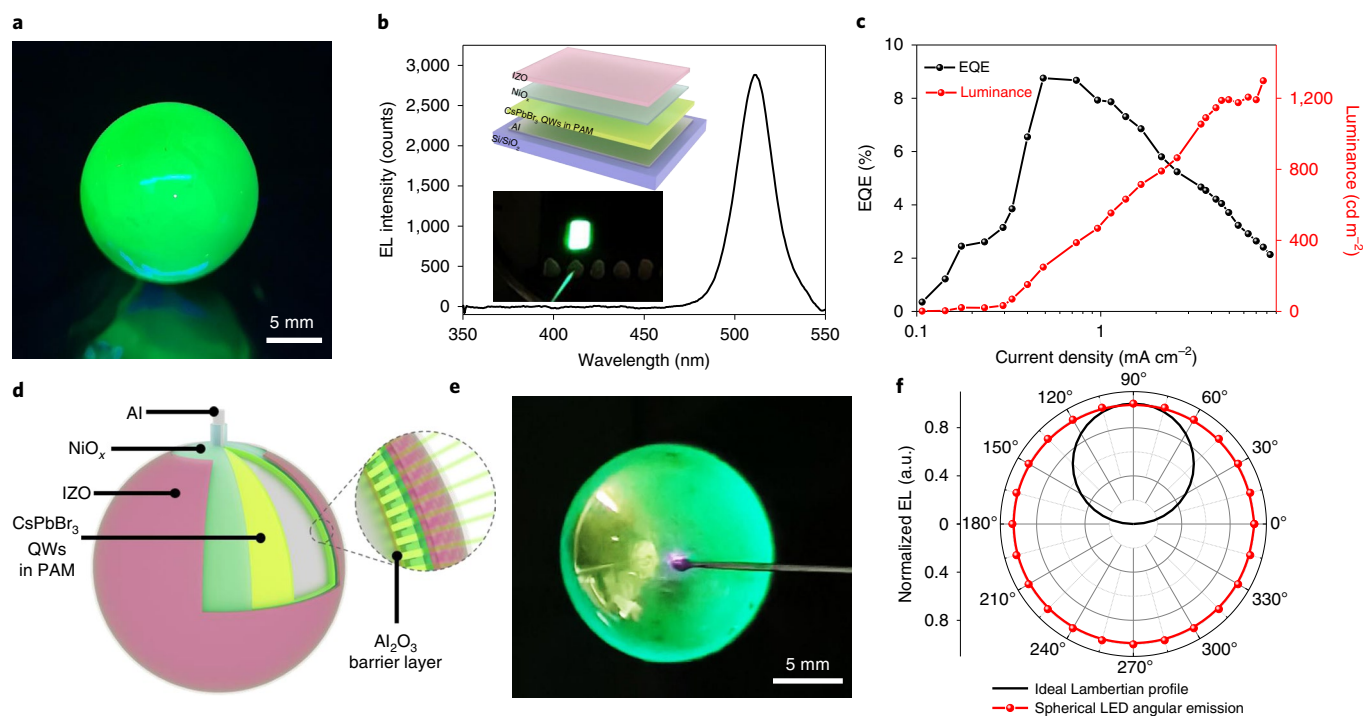
Fig. 6 | CsPbBr₃-QW-array-based LED performance. a, PL image of CsPbBr₃ QWs grown on an Al sphere. **b,c**, Planar device characterization: EL spectrum (**b**) and EQE–L–J (**c**) curves. The insets in **b** show the schematic (top) and EL image (bottom) of the planar device. The device size is 2.0 mm × 2.8 mm. **d**-**f**, Three-dimensional spherical device characterization: schematic (**d**), EL image (**e**) and angular emission profile (**f**) of a 3D spherical device under 10 V bias.

The *J–V* characteristics of this device are shown in Supplementary Fig. 24. The EQE–L–J curves of a planar device are shown in Fig. 6c. Intriguingly, the maximum EQE is improved to 8.76% compared with MAPbBr₃ QWs, and the luminance can reach 1,300 cd m⁻², which can be further improved by applying an electron transport layer (such as TPBi) to the MIS junction. To fabricate the 3D spherical LED device, normal IZO sputtering is changed to a two-axis rotation deposition (Supplementary Video 3) to achieve spatially uniform IZO electrode deposition on the sphere. A schematic of the 3D spherical device structure is demonstrated in Fig. 6d. Figure 6e shows the EL image of the 3D spherical LED under 10 V bias with uniform luminance (the yellow shadow is from the background light reflection). Further, the angular emission profile is shown in Fig. 6f, in comparison with an ideal Lambertian emission profile for common planar LEDs. This result shows that the 3D spherical LED has excellent spatial luminance uniformity, which makes it promising for future lighting applications with further optimization.

Discussion

Overall, our work opens up an alluring possibility to fabricate true 3D large-area and uniform perovskite films made of crystal-line QWs with high full-colour luminescence efficiency, excellent mechanical and environmental stability, and good flexibility. The 92% PLQY and 5,644 h T_{PL50} in ambient air without any encapsulation are good starting points for further optimization, combining material engineering and/or an additional packaging layer. It is worth mentioning that 3D large-area QWs themselves as well as QW-based 3D LEDs are highly promising for future large-area displays and unconventional lighting applications.

Online content

Any methods, additional references, Nature Research reporting summaries, source data, extended data, supplementary

information, acknowledgements, peer review information; details of author contributions and competing interests; and statements of data and code availability are available at https://doi.org/10.1038/s41566-022-00978-0.

References

1. Stranks, S. D. & Snaith, H. J. Metal-halide perovskites for photovoltaic and light-emitting devices. *Nat. Nanotechnol.* **10**, 391–402 (2015).
2. Xiao, Z. G. et al. Efficient perovskite light-emitting diodes featuring nanometre-sized crystallites. *Nat. Photon.* **11**, 108–115 (2017).
3. Cho, H. et al. Overcoming the electroluminescence efficiency limitations of perovskite light-emitting diodes. *Science* **350**, 1222–1225 (2015).
4. Liu, F. et al. Highly luminescent phase-stable CsPbI₃ perovskite quantum dots achieving near 100% absolute photoluminescence quantum yield. *ACS Nano* **11**, 10373–10383 (2017).
5. Deng, W. et al. Organic–inorganic hybrid perovskite quantum dots for light-emitting diodes. *J. Mater. Chem. C* **6**, 4831–4841 (2018).
6. Liu, Y. et al. Efficient blue light-emitting diodes based on quantum-confined bromide perovskite nanostructures. *Nat. Photon.* **13**, 760–764 (2019).
7. Lin, K. et al. Perovskite light-emitting diodes with external quantum efficiency exceeding 20 per cent. *Nature* **562**, 245–248 (2018).
8. Richter, J. M. et al. Enhancing photoluminescence yields in lead halide perovskites by photon recycling and light out-coupling. *Nat. Commun.* **7**, 13941 (2016).
9. Berhe, T. A. et al. Organometal halide perovskite solar cells: degradation and stability. *Energy Environ. Sci.* **9**, 323–356 (2016).
10. Zhang, D. et al. Ultrathin colloidal cesium lead halide perovskite nanowires. *J. Am. Chem. Soc.* **138**, 13155–13158 (2016).
11. Teunis, M. B. et al. Mesoscale growth and assembly of bright luminescent organolead halide perovskite quantum wires. *Chem. Mater.* **28**, 5043–5054 (2016).
12. Tan, C. K. & Tansu, N. Nanostructured lasers: electrons and holes get closer. *Nat. Nanotechnol.* **10**, 107–109 (2015).

13. Zhang, D. et al. Increasing photoluminescence quantum yield by nanophotonic design of quantum-confined halide perovskite nanowire arrays. *Nano Lett.* **19**, 2850–2857 (2019).
14. Yuen, P. Y., Moffitt, S. L., Novoa, F. D., Schelhas, L. T. & Dauskardt, R. H. Tearing and reliability of photovoltaic module backsheets. *Prog. Photovolt. Res. Appl.* **27**, 693–705 (2019).
15. Rolston, N. et al. Effect of cation composition on the mechanical stability of perovskite solar cells. *Adv. Energy Mater.* **8**, 1702116 (2018).
16. Gu, L. et al. 3D arrays of 1024-pixel image sensors based on lead halide perovskite nanowires. *Adv. Mater.* **28**, 9713–9721 (2016).
17. Waleed, A. et al. Lead-free perovskite nanowire array photodetectors with drastically improved stability in nanoengineering templates. *Nano Lett.* **17**, 523–530 (2017).
18. Waleed, A. et al. All inorganic cesium lead iodide perovskite nanowires with stabilized cubic phase at room temperature and nanowire array-based photodetectors. *Nano Lett.* **17**, 4951–4957 (2017).
19. Gu, L. et al. Significantly improved black phase stability of $FAPbI_3$ nanowires via spatially confined vapor phase growth in nanoporous templates. *Nanoscale* **10**, 15164–15172 (2018).
20. Soeda, J. et al. High electron mobility in air for *N,N'*-1*H*,1*H*-perflu orobutyldicyanoperylene carboxydi-imide solution-crystallized thin-film transistors on hydrophobic surfaces. *Adv. Mater.* **23**, 3681 (2011).
21. Diggle, J. W., Downie, T. C. & Goulding, C. Anodic oxide films on aluminum. *Chem. Rev.* **69**, 365–405 (1969).
22. Simmons, J. G. Generalized formula for the electric tunnel effect between similar electrodes separated by a thin insulating film. *J. Appl. Phys.* **34**, 1793–1803 (1963).
23. Li, J. et al. Perovskite light-emitting devices with a metal–insulator–semiconductor structure and carrier tunnelling. *J. Mater. Chem. C* **5**, 7715–7719 (2017).
24. Kam, M. et al. Efficient mixed-cation mixed-halide perovskite solar cells by all-vacuum sequential deposition using metal oxide electron transport layer. *Sol. RRL* **3**, 1900050 (2019).
25. Eames, C. et al. Ionic transport in hybrid lead iodide perovskite solar cells. *Nat. Commun.* **6**, 7497 (2015).
26. Lee, H., Ko, D. & Lee, C. Direct evidence of ion-migration-induced degradation of ultrabright perovskite light-emitting diodes. *ACS Appl. Mater. Interfaces* **11**, 11667–11673 (2019).
27. Tan, Z. F. et al. Spectrally stable ultra-pure blue perovskite light-emitting diodes boosted by square-wave alternating voltage. *Adv. Optical Mater.* **8**, 1901094 (2020).
28. Liu, J. J. et al. All-inorganic perovskite quantum dots/p-Si heterojunction light-emitting diodes under d.c. and a.c. driving modes. *Adv. Optical Mater.* **6**, 1700897 (2018).
29. Park, S. et al. Efficient large-area transparent OLEDs based on a laminated top electrode with an embedded auxiliary mesh. *ACS Photonics* **4**, 1114–1122 (2017).
30. Cheng, T., Wu, Y., Shen, X., Lai, W. & Huang, W. Inkjet printed large-area flexible circuits: a simple methodology for optimizing the printing quality. *J. Semicond.* **39**, 015001 (2018).

Methods

Materials. All the chemicals were purchased from Sigma-Aldrich and used as received without further purification.

PAM fabrication. PAMs were fabricated using a low-voltage anodic anodization method. Briefly, different d.c. voltages (5, 10 and 20 V) were used to generate different pore sizes (around 6, 12 and 20 nm) on an Al chip in an acid solution (5 vol% H_2SO_4) at 10 °C for different times (20, 10 and 1 min for 5, 10 and 20 V anodization, respectively). For pore sizes of 50 and 280 nm, oxalic acid (0.2 M in water) and a mixture solution of deionized water, ethylene glycol and H_3PO_4 (200:100:1 in volume) were used for 60 and 200 V anodization, respectively. The thickness of PAM was controlled by the anodization time. Except for the 5 V sample, a barrier-thinning process was carried out to reduce the barrier thickness[13]. Subsequently, the metallic Pb precursor was electrodeposited using a sinusoidal voltage signal with 50 Hz frequency and 5 V amplitude. Note that the PAM growth on Al sphere followed the same processes described above, except that an ultrahigh-purity (>99.99%) Al sphere with a diameter of 1.5 cm was used.

CSVR growth of perovskite QWs. $MAPbBr_3$ QW growth in the PAM was carried out using a CSVR process. Specifically, the PAM chip with deposited Pb and MABr powder were separately put into two face-to-face vertically stacked glass dishes. The distance between the chip and powder was around 2 cm. Then, these two face-to-face dishes were placed in a calibrated oven at a temperature of 180 °C for 2–5 h. No inert gas was needed in the oven. After that, the chip was taken out from the oven and cooled down to room temperature in ambient air. Mixed-halide-perovskite-based QWs were grown using mixed halide sources. Specifically, to obtain blue- and cyan-emission QWs, a mixture of MACl and MABr powders with different molar ratios were used. For red-emission QWs, the source was changed to a mixture of MABr and MAI with the same growth temperature and time. The growth of $CsPbBr_3$ QWs followed a similar process, except that the powder was changed to a mixture of CsBr and $PbBr_2$ with a molar ratio of 3:1 after 430 °C annealing in air for 1 h. CSVR growth for $CsPbBr_3$ was carried out under a temperature of 400 °C and pressure of 5×10^{-2} torr. After growth for 2 h, the system was naturally cooled down for another 2 h before taking out the chip. For the growth of $CsPbBr_3$ QWs on Al spheres, a two-zone furnace (independently temperature programmable) was used instead of one heating zone. The powder source and Al sphere were placed in the upstream and downstream heating zones, respectively, with both temperatures set at 400 °C. The growth pressure and time were the same as that of the planar chips. On successful growth, the Al sphere started to naturally cool down 20 min earlier than the powder source, preventing the decomposition of $CsPbBr_3$ QWs.

MAPbBr$_3$ thin-film fabrication. As the control sample, $MAPbBr_3$ thin film was fabricated using a two-step thermal evaporation method, which was reported to yield better humidity and mechanical stability than the spin-coated counterparts[24]. Briefly, $PbBr_2$ and MABr sources were located at the bottom of the evaporator chamber (with an angle of 90° with respect to the clean ITO substrate) and evaporated at a deposition rate in the range of 1.5–2.0 Å s^{-1}. Further, 33 nm $PbBr_2$ and 66 nm MABr were deposited to generate around 100 nm $MAPbBr_3$ film. The as-deposited films were annealed at 130 °C for 10 min in ambient air.

Hydrophobic treatment. To generate surface hydrophobicity, the surface of the PAM template was modified with fluorinated silanes (triethoxy-1H,1H,2H,2H-tridecafluoro-n-octylsilane) using a well-established protocol[20]. Briefly, the PAM chip was functionalized by chemical vapour deposition of the fluorinated silanes at 130 °C for 30 min. After that, the surface-functionalized PAM chip was baked at 130 °C for another 30 min on a hot plate to evaporate the excess materials.

Mechanical stability test. To test the adhesion force between the perovskite and substrate, a Kapton tape-assisted peel-off process was carried out on both QWs/PAM and thin-film/ITO samples. A schematic of the test setup is demonstrated in Fig. 3a. A pressure of around 2 N cm^{-2} was used to strengthen the adhesion between the tape and perovskite layer. Then, a fresh tape was used for the peel-off test and the PL spectrum was measured after every peel-off cycle. For calculating the cohesion energy G_c, the load (P)–displacement (Δ) curve was measured by a double-cantilever-beam system, as reported previously[15]. Then, G_c was calculated as follows[31]:

$$G_c = \frac{12 P_c^2 a^2}{B^2 E' h^3} \left(1 + 0.64 \frac{h}{a} \right),\qquad(1)$$

where P_c is the critical load applied at which crack growth occurs; a is the crack length; B and h are the width and half-thickness of the double-cantilever-beam specimen, respectively; and E' is the plane strain elastic modulus of the substrates. An estimation of the crack length was experimentally determined from the load–displacement curve, using the compliance relationship show in equation (2).

$$a = \left(\frac{\mathrm{d}\Delta}{\mathrm{d}P} \times \frac{BE' h^3}{8} \right)^{\frac{1}{3}} - 0.64 \times h\qquad(2)$$

The testing for G_c was carried out in ambient air. The specimen was loaded under tension with a displacement rate of 0.1 mm min^{-1}.

Fabrication of MAPbBr$_3$-QW-based LED devices. A layer of 300 nm pure Al was sputtered on a Si/SiO$_2$ wafer using a Varian 3180 sputtering system (SPT-3180). Afterwards, anodic anodization, Pb electrodeposition and CSVR process were carried out. After finishing the growth of QWs, a gentle ion-milling process was conducted on the chip surface to remove the surface bulk $MAPbBr_3$. Specifically, positive Ar ions were obtained and accelerated to mill the chip surface by 100 V acceleration voltage in a vacuum chamber (1.4×10^{-4} torr). The angle between the ion path and normal of the chip is 80°. The chip was continuously rotated and cooled during the milling period. Afterwards, another short (10 min) CSVR process with the same growth conditions was carried out to repair the ion-beam-damaged surface. Finally, a CuPc layer (20 nm) and an IZO layer (200 nm) were thermally evaporated at a rate of 0.4 Å s^{-1} and magnetically sputtered at a rate of 0.3 Å s^{-1}, respectively. Note that the unique low-deposition-rate IZO sputtering was achieved with low radio-frequency power (50 W) and extremely low working pressure (2×10^{-2} Pa) to avoid sputtering damage to the underlying materials. For large-scale device fabrication, the thickness of the bottom Al was increased to 1 μm for better current injection. To achieve patterned EL, a shadow mask was used during IZO deposition. Another shadow mask (Supplementary Fig. 20) was utilized for depositing the Au gridline electrodes, with 90° displacement between two successive evaporation steps. To make a flexible device, the IZO layer was changed to 30 nm Au that was thermally evaporated on CuPc at a deposition rate of 4 Å s^{-1}.

Fabrication of CsPbBr$_3$-QW-based LEDs. For fabricating $CsPbBr_3$ QW LEDs, NiO_x thin film was deposited by ALD as the HTL. The ALD process was carried out in an ALD system (MNT-S100Oz-L6S2, JiangSu MNT Micro and Nano tech). The system contained a reaction chamber with separated gas channels for Ni(dmamb)$_2$ and O$_3$ (which was generated from O$_2$). The chamber and Ni(dmamb)$_2$ source were heated up to 100 and 130 °C, respectively, before deposition. Nitrogen was used as the carrier gas for both Ni(dmamb)$_2$ and O$_3$. The base pressure of the chamber during the ALD process was ~20 Pa. One completed ALD cycle contained the following five successive steps: Ni(dmamb)$_2$ pulse (1.5 s), waiting (5.0 s), Ni(dmamb)$_2$ purge (20.0 s), O$_3$ pulse (1.0 s) and O$_3$ purge (20.0 s). Note that NiOOH was produced after the ALD process; post-annealing under 300 °C in air was carried out to convert it to NiO_x. Typically, 200 cycles were proceeded to obtain ~20 nm NiO_x film as the HTL. To fabricate the top transparent electrode, normal IZO sputtering was carried out on top of NiO_x for the planar device. For the spherical device, a two-axis rotation of the Al sphere was added during sputtering to obtain a spatially uniform IZO electrode on the spherical device (Supplementary Video 3).

Characterization. SEM images were characterized using field-emission scanning electron microscopy (JEOL JSM-7800F). XRD patterns were obtained using a Bruker D8 X-ray diffractometer. TEM images were obtained by a TEM JEOL instrument (2010F) with 200 kV acceleration voltage. UV–visible absorption and PL spectra including the lifetime were measured using a Varian Cary 500 spectrophotometer (Varian) and FS5 fluorescence spectrometer (Edinburgh Instruments), respectively. PL stability of the QWs was demonstrated by measuring the PL spectrum once every few hours; each time, the QWs were only exposed to a light source (350 nm and 5 mW cm^{-2}) for 30 s to avoid UV-induced degradation. The PLQY was measured using a custom-built micro-PL instrument reported earlier[32]. A HELIOS femtosecond TA spectrometer (Ultrafast Systems) was used for TA measurements, which was mainly based on a regenerative amplified Ti:sapphire pulsed laser from Coherent Legend (wavelength of 800 nm, pulse of 150 fs, energy of 5 mJ per pulse and repetition rate of 1 kHz). Briefly, the 800 nm output pulsed laser from the amplifier was split into two parts with a beamsplitter. Here 75% of the output light was used to generate a frequency-doubled (400 nm) pumping light with the utilization of a BaB_2O_4 crystal. The left portion of the output laser was concentrated into a sapphire window to generate a white-light continuum from 420 to 780 nm and used as the probe light. The 400 nm pumping light was focused at the sample with a beam diameter of ~360 μm and beam power density of 40 μJ cm^{-2}. LED characterization was done using an Ocean Optics Flame spectrometer and an integrating sphere with the method reported in a previous work[33].

Data availability

The data that support the findings of this study are available from the corresponding author upon reasonable request.

References

31. Kanninen, M. An augmented double cantilever beam model for studying crack propagation and arrest. *Int. J. Fract.* **9**, 83–92 (1973).
32. Amani, M. et al. Near-unity photoluminescence quantum yield in MoS$_2$. *Science* **350**, 1065–1068 (2015).

33. Zhang, Q. et al. Efficient metal halide perovskite light-emitting diodes with significantly improved light extraction on nanophotonic substrates. *Nat. Commun.* **10**, 727 (2019).

Acknowledgements

Author contributions

Competing interests

The authors declare no competing interests.

Additional information

Supplementary information The online version contains supplementary material available at https://doi.org/10.1038/s41566-022-00978-0.

Correspondence and requests for materials should be addressed to Zhiyong Fan.

Peer review information *Nature Photonics* thanks Qihua Xiong and the other, anonymous, reviewer(s) for their contribution to the peer review of this work.

Reprints and permissions information is available at www.nature.com/reprints.